Nanoscale Advances

ROYAL SOCIETY OF CHEMISTRY

PAPER

View Article Online
View Journal | View Issue

Cite this: *Nanoscale Adv.*, 2026, **8**, 1748

Rosette-shaped $Co_2Mn_3O_8$ integrated with nanoflower-like Mn–Co LDH anchored on rGO sheets: a bifunctional electrode for advanced supercapacitors and oxygen evolution reaction (OER)

Sammar Min Allah,[a] Muhammad Kashif Aslam, *[a] Iftikhar Hussain, [c] Muhammad Ehtasham ul-Haq,[d] Ali H. Al-Marzouqi*[a] and Maowen Xu *[b]

Mn–Co layered double hydroxide (LDH) is a promising electrode material for supercapacitor and oxygen evolution reaction (OER) applications due to its unique layered structure with Mn and Co active sites. However, its full potential for supercapacitor and OER applications is underutilized due to its low conductivity and limited availability of active sites. The challenges related to the super capacitive and OER properties of Mn–Co LDH are overcome by combining it with highly redox-active $Co_2Mn_3O_8$ and highly conductive rGO to form the Mn–Co LDH/rGO/$Co_2Mn_3O_8$ composite. The hierarchical rosette- and nanoflower-like Mn–Co LDH/rGO/$Co_2Mn_3O_8$ composite is prepared using a hydrothermal method followed by calcination. Characterization using FESEM, XRD, XPS, and Raman spectroscopy reveals a unique morphology that enhances conductivity and results in improved performance for supercapacitor and OER applications. As a result, the Mn–Co LDH/rGO/$Co_2Mn_3O_8$ composite demonstrates a high specific capacitance of 2500 F g^{-1} at 1 A g^{-1} in a 3 M KOH electrolyte. Furthermore, the asymmetric supercapacitor (ASC) device employing Mn–Co LDH/rGO/$Co_2Mn_3O_8$ delivers an energy density of 32 Wh kg^{-1} at a power density of 600 W kg^{-1}. The zinc-ion supercapacitor based on Mn–Co LDH/rGO/$Co_2Mn_3O_8$ achieves an impressive energy density of 100 Wh kg^{-1} at a power density of 780 W kg^{-1}. Additionally, Mn–Co LDH/rGO/$Co_2Mn_3O_8$ performs well for the OER, exhibiting a low overpotential of 218 mV (at 10 mA cm^{-2}) and a small Tafel slope of 56.03 mV dec^{-1} in 0.1 M KOH. This study opens promising prospects for the dual utilization of Mn–Co LDH/rGO/$Co_2Mn_3O_8$ in supercapacitor and OER applications.

Received 9th November 2025
Accepted 27th January 2026

DOI: 10.1039/d5na01043h

rsc.li/nanoscale-advances

1. Introduction

The deleterious impact of climate change caused by the continuous consumption of fossil fuels has accelerated the transition towards clean energy resources such as solar, wind, and hydropower.[1–5] However, due to the intermittent nature of these clean energy sources, their utilization is ineffective without the development of efficient energy storage devices.[6–10] Supercapacitors offer a unique opportunity to store energy from clean energy sources due to their higher power density than that of batteries.[11–13] However, their major disadvantage is low energy density, which limits their applications. Therefore, designing suitable materials for supercapacitor electrodes can help circumvent the problem of low energy density.[14,15] Additionally, water splitting, which combines the oxygen evolution reaction (OER) and hydrogen evolution reaction (HER), represents a promising process for alleviating the energy crisis through efficient energy conversion.[16–18] The sluggish kinetics of the OER is a major hindrance to water splitting.[19–21] Therefore, it is imperative to develop suitable bifunctional electrode materials that not only enhance the energy density of supercapacitors but also overcome the sluggish OER kinetics, thereby solving the challenges in energy storage and energy conversion.[22]

Recently, layered double hydroxides (LDHs) have attracted widespread attention for their applications in energy storage and conversion.[23,24] The unique properties of LDHs arise from their layered structure, in which the divalent (M^{2+}) and trivalent (M^{3+}) metal ions are interconnected through hydroxide (OH^-)

[a]*Department of Chemical and Petroleum Engineering, UAE University, PO BOX 15551, Al Ain, United Arab Emirates. E-mail: hassana@uaeu.ac.ae; aslam_kashif@outlook.com*

[b]*Chongqing Key Laboratory of Battery Materials and Technologies, School of Materials & Energy, Southwest University, Chongqing 400715, P.R. China. E-mail: xumaowen@swu.edu.cn*

[c]*Department of Mechanical Engineering, City University of Hong Kong, 83 Tat Chee Avenue, Kowloon, Hong Kong*

[d]*School of Chemistry and Chemical Engineering, Nanjing University of Science and Technology, 210094 Nanjing, Jiangsu, China*

groups, forming positively charged layers.[25] Anions and water molecules are located between the layers to maintain charge neutrality and structural stability.[26] As a result of this structure, many active sites are available, providing LDHs with bi-functionality—enabling redox activity for the oxygen evolution reaction (OER) and pseudo capacitance for energy storage.[27,28] Among various LDHs, Mn–Co LDH has been extensively utilized for energy storage and conversion due to its large number of active sites and well-structured architecture.[29] As a result, electrolyte ion transport toward the LDH experiences minimal resistance, leading to enhanced performance in both the oxygen evolution reaction (OER) and supercapacitor applications.[30,31] For example, Su *et al.* synthesized Co–Mn LDH nanoneedles grown on Ni foam for supercapacitor applications, which demonstrated an excellent specific capacitance of 2422 F g^{-1} at a current density of 1 A g^{-1}.[32] Xuan *et al.* synthesized MnCo-LDH/rGO@$NiCo_2S_4$ heterostructures supported on Ni foam, which exhibited a high specific capacitance of 1446.5C g^{-1} at a current density of 1 A g^{-1}.[33] Liu *et al.* synthesized hierarchical MnCo-layered double hydroxide@$Ni(OH)_2$ core–shell heterostructures, which displayed a superior specific capacitance of 2320 F g^{-1} at a current density of 3 A g^{-1}.[34] Zain Ul *et al.* synthesized MnCo-LDH@NiP_2 and MnCo-LDH@Ni_5P_4, which showed remarkable OER activity, with overpotentials of 276 mV and 318 mV, respectively, at a current density of 100 mA cm^{-2}.[35] Ma *et al.* synthesized CoFe-LDH@MnCo-CH nanoneedle arrays, which demonstrated excellent performance with a low overpotential of 250 mV at a current density of 10 mA cm^{-2}.[36] Li *et al.* synthesized three-dimensional graphene-like carbon nanosheets coupled with MnCo-layered double hydroxide nanoflowers, achieving an overpotential of 370 mV at a current density of 10 mA cm^{-2}.[37] Despite the widespread use of Mn–Co LDH, its performance in supercapacitors and the oxygen evolution reaction (OER) still faces certain drawbacks.[38,39] The most common limitation of Mn–Co LDH is its low electrical conductivity, which reduces specific capacitance and increases overpotential in OER applications, respectively.[40,41] Furthermore, due to the relatively weak structure of Mn–Co LDH, it suffers from volume changes, which limit its further application in supercapacitors and OER.[42] Therefore, designing suitable composites by incorporating appropriate materials with Mn–Co LDH to enhance its performance in energy conversion and storage is essential.

Bimetallic oxides offer numerous advantages for improving the performance of LDH for supercapacitor and OER applications.[43] Various bimetallic oxides, such as $CuMoO_4$ and $Ni_2Co_2O_4$, have been extensively utilized for energy storage and conversion.[44] For example, MinAllah *et al.* synthesized $CuMoO_4$ urchins for supercapacitor applications, demonstrating 2200 F g^{-1} at 1 A g^{-1}.[45] Similarly, $NiCo_2O_4$ surpassed many LDH materials for OER with a low overpotential of 360 mV at 10 mA cm^{-2}.[46] The superior electrocatalytic activity of bimetallic oxides arises from their structure, which is formed by the combination of bimetals and oxides.[47] Among various bimetallic oxides, $Co_2Mn_3O_8$ has emerged as a promising candidate for energy storage and conversion.[48,49] The multiple advantages of $Co_2Mn_3O_8$ include: (1) superior conductivity compared to LDH, (2) multiple redox-active sites that promote extraordinary electrocatalytic activity, and (3) a robust structure that imparts structural stability to compensate for the volume changes of LDH occurring during continuous cycling over long periods.[50] Therefore, the incorporation of $Co_2Mn_3O_8$ into Mn–Co LDH is expected to increase specific capacitance, lower the overpotential for OER, and improve cyclic stability. Furthermore, the addition of rGO to the composition will provide conductive pathways for electron transport, enhancing electrocatalytic performance. Therefore, the investigation of Mn–Co LDH/rGO/$Co_2Mn_3O_8$ represents a novel approach, as this material is expected to provide sufficient capacity to enhance the performance of Mn–Co LDH in OER and supercapacitor applications, which has not yet been reported in the literature.

Herein, a Mn–Co LDH/rGO/$Co_2Mn_3O_8$ composite was fabricated for supercapacitor and OER applications. Firstly, $Co_2Mn_3O_8$ was synthesized by the hydrothermal method, followed by calcination. Secondly, Mn–Co LDH/rGO/$Co_2Mn_3O_8$ was synthesized using the *in situ* hydrothermal method. Mn–Co LDH/rGO/$Co_2Mn_3O_8$, comprising rosette-like $Co_2Mn_3O_8$ integrated with nanoflower-like Mn–Co LDH through rGO nanosheets, was utilized as a supercapacitor electrode material and demonstrated a superior specific capacitance of 2500 Fg^{-1} at 1 Ag^{-1}. The Mn–Co LDH/rGO/$Co_2Mn_3O_8$-based asymmetric supercapacitor device (ASC) demonstrates an energy density of 32 Wh kg^{-1} at a power density of 600 W kg^{-1}. Furthermore, the Mn–Co LDH/rGO/$Co_2Mn_3O_8$-based zinc-hybrid supercapacitor demonstrated a superior energy density of 100 Wh kg^{-1} at a power density of 780 W kg^{-1}. The Mn–Co LDH/rGO/$Co_2Mn_3O_8$ utilized for OER demonstrated superior OER performance with a low overpotential of 218 mV and a Tafel slope of 56.03 mV dec^{-1}, respectively.

2. Experimental section

2.1. Synthesis of Mn–Co LDH

Briefly, 0.21 g of manganese(II) chloride tetrahydrate and 0.36 g of cobalt(II) nitrate hexahydrate were stirred in 70 mL of deionized water to obtain a uniformly mixed solution. To this solution, 0.72 g of urea was added and stirred for 5 minutes. The mixture was transferred to an autoclave and maintained at 100 °C for 5 h. Finally, it was washed three times with ethanol and water to obtain Mn–Co LDH nanoflowers.

2.2. Synthesis of $Co_2Mn_3O_8$

0.2975 g of cobalt(II) chloride hexahydrate was dissolved in a 5 : 20 volume ratio under stirring for 10 minutes. Then, 0.099 g of manganese(II) chloride was added to the mixture. Afterwards, 0.9 g of urea was added and stirred for 5 minutes. The mixed solution was transferred to an autoclave and maintained at 120 °C for 6 h. Afterwards, calcination was carried out at 350 °C for 3 h with a ramp rate of 4.5 °C min^{-1} to form rosette-like $Co_2Mn_3O_8$.

2.3. Synthesis of Mn–Co LDH/r-GO/$Co_2Mn_3O_8$

The as-prepared rosette-like $Co_2Mn_3O_8$ was dispersed in an r-GO mixture and further sonicated for 10 minutes using a probe sonicator to obtain a black-coloured dispersion. Afterwards, this dispersion was transferred to a beaker containing 0.21 g of manganese(II) chloride tetrahydrate and 0.36 g of cobalt(II) nitrate hexahydrate in 70 mL of deionized water. After complete mixing, the solution was transferred to an autoclave and maintained at 100 °C for 5 h. Finally, the rosette-like $Co_2Mn_3O_8$ integrated with nanoflower-like Mn–Co LDH through r-GO was obtained in the form of Mn–Co LDH/r-GO/$Co_2Mn_3O_8$.

2.4. Fabrication of the electrode material

The as-prepared Mn–Co LDH/r-GO/$Co_2Mn_3O_8$ was mixed with carbon black and PVDF in an 8 : 1 : 1 ratio. NMP was then added to this mixture, which was sonicated in a sonication bath for 30 minutes to obtain a uniform ink. The ink was spray-coated onto a 1 × 1 cm^2 piece of nickel foam, which was then dried in an oven overnight at 60 °C.

2.5. Characterizations

The morphological analysis of Mn–Co LDH/rGO/$Co_2Mn_3O_8$ was carried out using scanning electron microscopy (SEM), while its crystalline structure was examined using X-ray diffraction (XRD; Bruker D8 Advance A25, Co target, Kα_1 = 1.78897 Å, 0.02 mm thick Fe filter). The atomic composition of Mn–Co LDH/rGO/$Co_2Mn_3O_8$ was analysed using X-ray photoelectron spectroscopy (XPS; PHI 5000 VersaProbe). The molecular composition was examined using Raman spectroscopy (LabRAM HR Evolution with a 532 nm laser).

2.6. Electrochemical testing

The electrochemical analysis of Mn–Co LDH/rGO/$Co_2Mn_3O_8$ was performed using a CHI 760E potentiostat. A three-electrode configuration was employed, where Mn–Co LDH/rGO/$Co_2Mn_3O_8$ served as the working electrode, platinum foil as the counter electrode, and an Ag/AgCl electrode as the reference electrode. A 3 M KOH solution was used as the electrolyte in the three-electrode system. The effective area of the working electrode was 1 × 1 cm^2. The potential window for the CV analysis in the three-electrode system is −0.25 to 0.45 V. The galvanostatic charge–discharge (GCD) experiments were carried out at current densities ranging from 1 to 10 A g^{-1} within the specified potential window. Electrochemical impedance spectroscopy (EIS) was performed in the frequency range of 0.01 Hz to 100 kHz. The following equation was used to calculate the electrochemical parameters of the supercapacitor in a three-electrode system:

$$C = \frac{I \times \Delta t}{m \times \Delta V}$$

where C represents the specific capacitance in a three-electrode system in Farads per gram (Fg^{-1}). m represents the mass of Mn–Co LDH/rGO/$Co_2Mn_3O_8$ loaded in grams (g). I represents the current in Ampere (A). Δt represents the discharge time (s). ΔV represents the potential window in volts (V).

2.7. Electrochemical testing of ASC and zinc-ion supercapacitor devices

The ASC device was fabricated by spraying an ink prepared from a finely ground mixture of Mn–Co LDH/rGO/$Co_2Mn_3O_8$, PVDF, and carbon black in an 8 : 1 : 1 ratio onto a nickel foam using NMP as the solvent. The fabricated electrode was then dried overnight. The anode was fabricated by coating or spraying a mixture of carbon black and PVDF in a 9 : 1 ratio onto nickel foam. A 1 × 1 cm^2 filter paper was then sandwiched between the cathode and the anode to assemble the ASC device.

The zinc-ion supercapacitor was fabricated by sandwiching a filter paper soaked in 2 M $ZnCl_2$ between a zinc plate, serving as the anode, and the Mn–Co LDH/rGO/$Co_2Mn_3O_8$ cathode. For the two-electrode system (ASC and zinc-ion supercapacitor), the following relations were used:

$$E = \frac{0.5 \times C \times \Delta V^2}{3600} \times 1000$$

$$P = \frac{3600 \times E}{\Delta t}$$

where E represents the energy density (Wh kg^{-1}). P represents the power density (W kg^{-1}).

3. Results and discussion

3.1. Characterization of Mn–Co LDH/rGO/$Co_2Mn_3O_8$

Fig. 1(b) shows the FESEM images of Mn–Co LDH/rGO/$Co_2Mn_3O_8$. The Mn–Co LDH appears to grow in a nanoflower-like structure, likely due to the interaction between Mn and Co. The multiple petals of the nanoflower originate from the centre and extend outward in a unique fashion, creating distinct pathways for electrolyte ion transport, which contributes to enhancing the material's performance. The rGO sheets are clearly visible, stacked and arranged around the Mn–Co LDH. Additionally, the rosette-like $Co_2Mn_3O_8$ is integrated with Mn–Co LDH in the Mn–Co LDH/rGO/$Co_2Mn_3O_8$ composite, forming a 3D architecture. The rosette-like $Co_2Mn_3O_8$ further enhances the material's performance through its spike-like radiations extending in all directions. This unique morphology reduces electrolyte transport resistance by providing abundant channels. This morphology provides numerous active sites, thereby significantly enhancing the overall performance of the material. Fig. 1(c and d) depict the rosette-like morphology of $Co_2Mn_3O_8$ alongside the nanoflower morphology of Mn–Co LDH integrated with rGO sheets.

The crystalline phase of Mn–Co LDH/rGO/$Co_2Mn_3O_8$ was further confirmed using XRD, as shown in Fig. 1(e). XRD analysis was done in the 2θ range of 10°–80°. The peak at 25° corresponds to the (002) plane of rGO, while the peak at 45° corresponds to the (001) plane of rGO.[51] The peaks at 31°, 32°, 36°, and 37.8° correspond to the (112), (103), (211), and (212) planes of $Co_2Mn_3O_8$, respectively, matching well with its

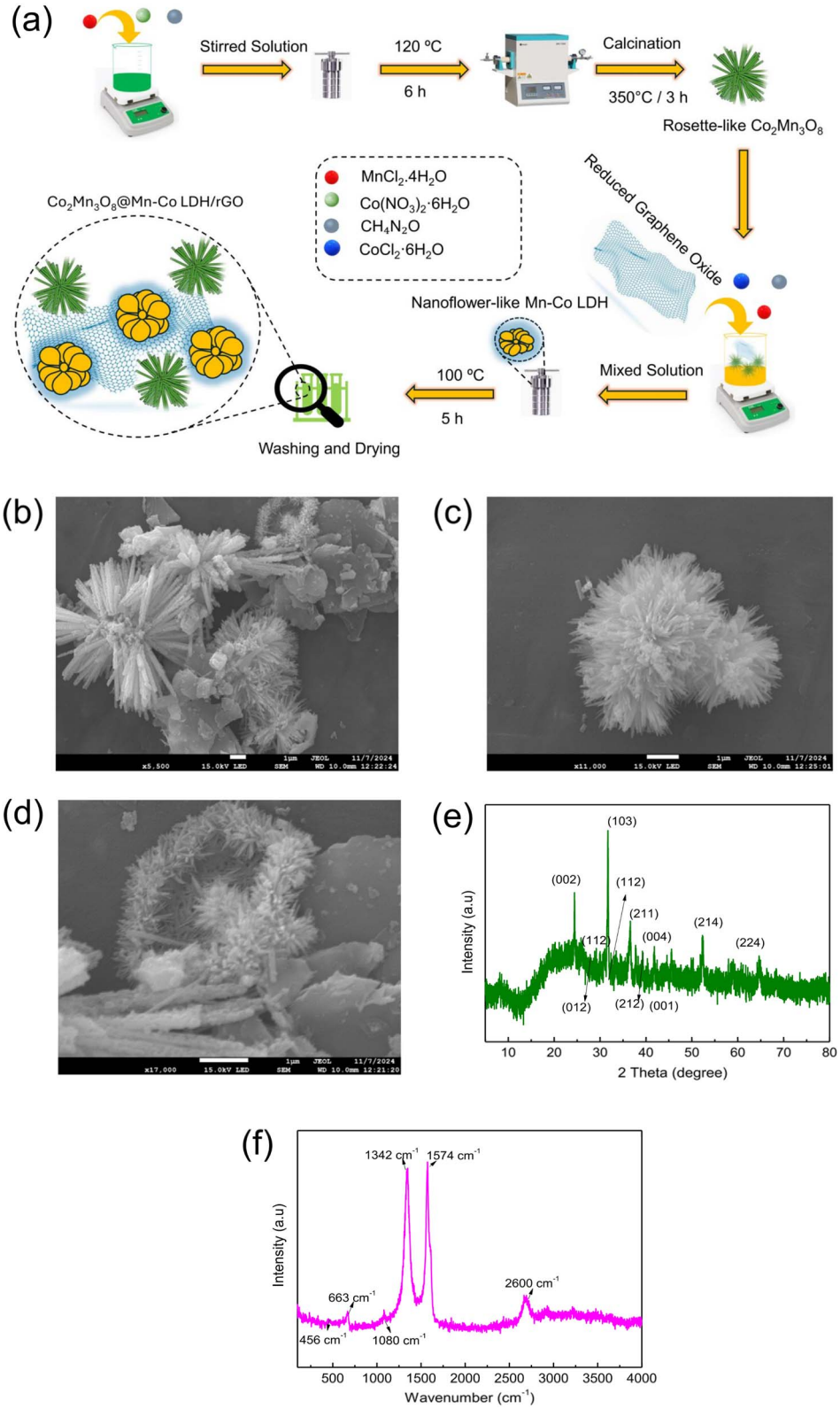

Fig. 1 (a) Schematic of the synthesis of Mn–Co LDH/rGO/$Co_2Mn_3O_8$, (b) SEM images of Mn–Co LDH/rGO/$Co_2Mn_3O_8$, (c) SEM images of $Co_2Mn_3O_8$, (d) SEM images of Mn–Co LDH/rGO, (e) XRD pattern of Mn–Co LDH/rGO/$Co_2Mn_3O_8$ and (f) Raman spectrum of Mn–Co LDH/rGO/$Co_2Mn_3O_8$.

standard XRD pattern.[52] Additionally, the peaks at 28.8°, 32°, 36°, 38°, and 59.8° correspond to the (112), (103), (211), (004), and (224) planes of Mn–Co LDH, serving as its characteristic fingerprints.[53] The molecular composition was further analysed using Raman spectroscopy, as shown in Fig. 1(f). The bands at 456, 663, and 1080 cm^{-1} correspond to the Co–O and Mo–O bonds in the composite.[54,55] The bands at 1342 and 1574 cm^{-1} correspond to the D and G bands of rGO, respectively. The band at 2600 cm^{-1} is attributed to Mo–O stretching.[56] Fig. 1(a) shows the schematic of the synthesis of Mn–Co LDH/rGO/$Co_2Mn_3O_8$. $Co_2Mn_3O_8$ was synthesized by a hydrothermal method, followed by calcination, and then integrated with rGO and dissolved in Mn–Co LDH. This process resulted in a rosette-shaped $Co_2Mn_3O_8$ integrated with the nanoflower-like Mn–Co LDH anchored on rGO sheets. Fig. 2(a) shows the high-resolution XPS spectrum of Co. The peaks exhibit bimodal characteristics corresponding to Co^{2+} and Co^{3+}. The XPS spectrum displays two broad peaks at 780.31 eV and 795.24 eV, corresponding to Co $2p_{3/2}$ and Co $2p_{1/2}$, respectively. Additionally, two satellite peaks appear at 787.0 eV and 803.0 eV. Fig. 2(b) shows the high-resolution spectrum of Mn in Mn–Co LDH/rGO/$Co_2Mn_3O_8$.[57,58] The peaks at 641 eV and 653 eV correspond to Mn $2p_{3/2}$ and Mn $2p_{1/2}$, respectively, confirming the presence of two spin–orbit components in the Mn spectrum.[57] Fig. 2(c) shows the XPS spectrum of C1 s in Mn–Co LDH/rGO/$Co_2Mn_3O_8$. The peak at 284 eV corresponds to the graphitic carbon of rGO present in the composite, while the peak at 286 eV represents the C–OH bonds in the rGO of Mn–Co LDH/rGO/$Co_2Mn_3O_8$.[58,59] The XPS spectrum of O 1s can be deconvoluted into three peaks, as shown in Fig. 2(d). The peaks at 529 eV, 531 eV, and 532 eV correspond to O_1, O_2, and O_3, respectively. These peaks are attributed to lattice termination, lattice oxygen, and adsorbed oxygen.[57,58]

3.2. Electrochemical characterizations

The electrochemical analysis of Mn–Co LDH/rGO/$Co_2Mn_3O_8$, conducted in the three-electrode system, is shown in Fig. 3. The CV analysis was performed at various scan rates, ranging from 2 mV s^{-1} to 100 mV s^{-1}, within a potential window of −0.25 to 0.45 V *vs.* Ag/AgCl, as shown in Fig. 3(a). Peaks 1, 2, 3, and 4 correspond to redox reactions due to the abundant active sites of Co^+ and Mo^+.[60] The shift of these anodic and cathodic peaks towards more positive and negative potentials, respectively,

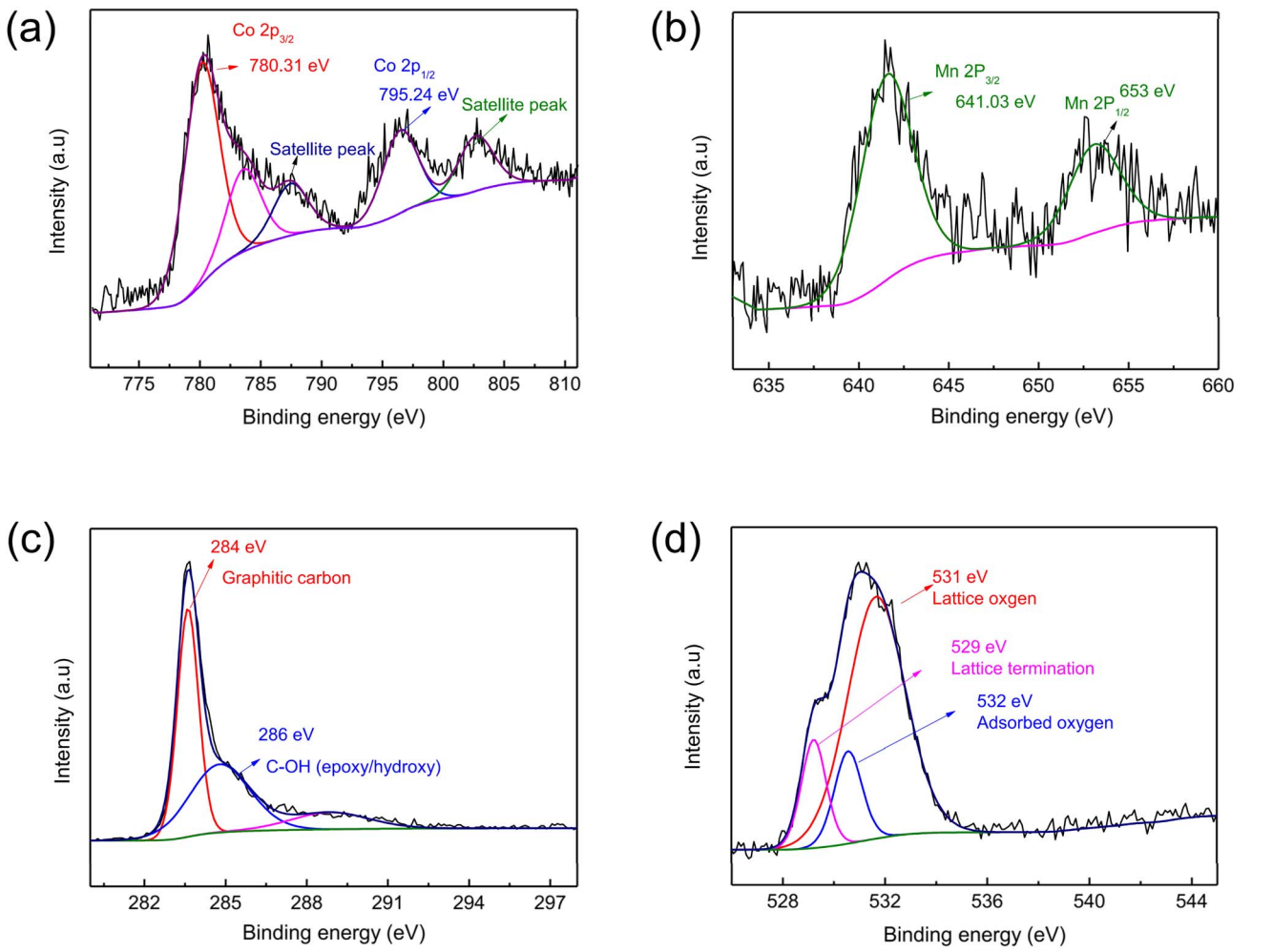

Fig. 2 XPS spectra of (a) Co 2p, (b) Mn 2p, (c) C 1s, and (d) O 1s.

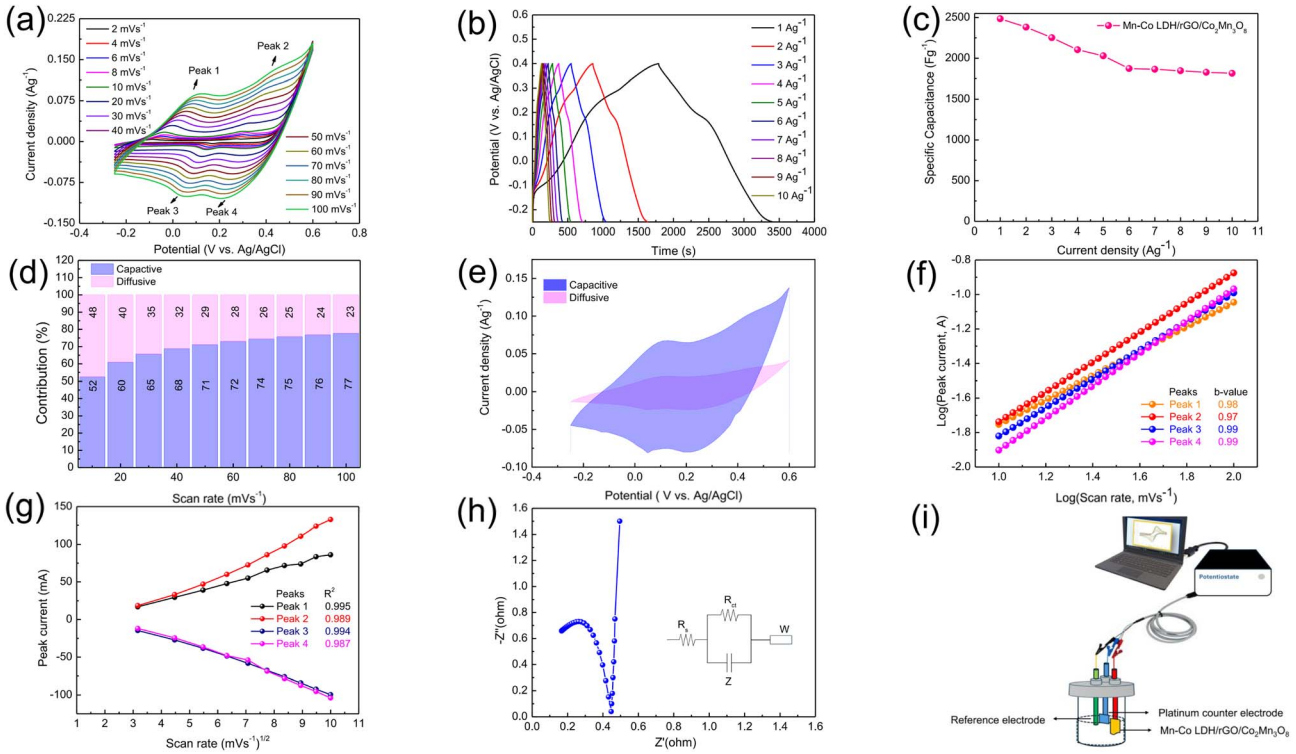

Fig. 3 Three-electrode testing of Mn–Co LDH/rGO/$Co_2Mn_3O_8$: (a) CV curves of Mn–Co LDH/rGO/$Co_2Mn_3O_8$ at various scan rates, (b) GCD curves of Mn–Co LDH/rGO/$Co_2Mn_3O_8$, (c) specific capacitances of Mn–Co LDH/rGO/$Co_2Mn_3O_8$ at various current densities, (d) Dunn method analysis of Mn–Co LDH/rGO/$Co_2Mn_3O_8$, (e) capacitive *vs.* diffusive contribution at 100 mV s^{-1}, (f) *b*-values of peak 1, peak 2, peak 3, and peak 4 of Mn–Co LDH/rGO/$Co_2Mn_3O_8$, (g) R^2-analysis for peak 1, peak 2, peak 3, and peak 4, (h) EIS spectra and equivalent circuit fitting for Mn–Co LDH/rGO/$Co_2Mn_3O_8$, and (i) schematic of Mn–Co LDH/rGO/$Co_2Mn_3O_8$.

indicates the presence of polarization resistance.[61] The CV of Mn–Co LDH/rGO/$Co_2Mn_3O_8$ exhibits a consistent shape at different scan rates, confirming the reversibility of the Mn–Co LDH/rGO/$Co_2Mn_3O_8$ electrode during multiple CV cycles.[62] Fig. 3(b) shows the GCD curve of Mn–Co LDH/rGO/$Co_2Mn_3O_8$ recorded in the potential range of −0.25 to 0.45 V *vs.* Ag/AgCl.[60] The GCD curve confirms the presence of redox behaviour, as evidenced by humps during charge–discharge processes, consistent with the CV results. The specific capacitance calculated from the GCD curves is shown in Fig. 3(c). Mn–Co LDH/rGO/$Co_2Mn_3O_8$ delivers a specific capacitance of 2500 F g^{-1} at 1 A g^{-1}. The enhancement in the specific capacitance of Mn–Co LDH/rGO/$Co_2Mn_3O_8$ is also attributed to the addition of rGO, alongside the rosette-like $Co_2Mn_3O_8$ and nanoflower-like Mn–Co LDH morphologies. The rGO improves specific capacitance due to its high electrical conductivity, which facilitates redox reactions. The increased capacitance is also attributed to the presence of carbonyl and hydroxyl groups on the rGO surface, as revealed by XPS analysis (Fig. 2(c)). Additionally, the rGO sheets provide unique pathways connecting the rosette-like $Co_2Mn_3O_8$ and nanoflower-like Mn–Co LDH morphologies, thereby facilitating the electrolyte ion transport with minimal resistance. Therefore, the combined effects of the morphology of Mn–Co LDH/rGO/$Co_2Mn_3O_8$ on improving the specific capacitance are as follows: (1) the rosette-like $Co_2Mn_3O_8$ provides abundant active sites, facilitating pseudocapacitive behaviour, (2) the nanoflower-like Mn–Co LDH enhances electrolyte ion transport, minimizes electrolyte resistance, and provides additional Mn and Co active sites. (3) The rGO sheets interconnect $Co_2Mn_3O_8$ and Mn–Co LDH, improving both electrical conductivity and structural stability. Furthermore, the specific capacitance decreases with increasing current density, which is consistent with trends reported in the literature.[63] The capacitive and diffusive contributions of Mn–Co LDH/rGO/$Co_2Mn_3O_8$ were analysed at different scan rates using Dunn's method.[64] The charge storage mechanism is governed by a combination of (1) charge transfer at the electrode–electrolyte interface, (2) faradaic charge transfer, and (3) non-faradaic charge transfer.[65] The capacitive contribution increases with scan rate. Specifically, the capacitive contribution was 52%, 60%, 65%, 68%, 71%, 72%, 74%, 75%, 76%, and 77% at scan rates of 10, 20, 30, 40, 50, 60, 70, 80, 90, and 100 mV s^{-1}, respectively. The diffusive contribution was 48%, 40%, 35%, 32%, 29%, 28%, 26%, 25%, 24%, and 23% at the corresponding scan rates, respectively. Fig. 3(e) shows the capacitive current and diffusive current contributions at 100 mV s^{-1}. This suggests that the capacitive contribution dominates over the diffusive contribution. The *b*-values for peak 1, peak 2, peak 3, and peak 4 are shown in Fig. 3(f). The following formula was used for the calculation of *b*-values for these peaks:[66]

$$i = av^b$$

A fully capacitive-controlled process is governed by *a b*-value of 0.5, while a *b*-value of 1 represents a diffusive-controlled process. When the charge storage has *b*-values between 0.5 and 1, it reflects that the charge storage is governed by a combination of both diffusive and capacitive processes.[67] All peaks (peak 1, peak 2, peak 3, and peak 4) have *b*-values between 0.5 and 1, which reflects that the process is governed by both diffusive and capacitive charge storage. To further confirm the charge-transfer process, the R^2 values for peak 1, peak 2, peak 3, and peak 4 were calculated by plotting the peak current *versus* (scan rate)$^{0.5}$.[68] The R^2 values for peak 1, peak 2, peak 3, and peak 4 were 0.995, 0.989, 0.994, and 0.987, respectively. This suggests that the process is dominated by a combination of diffusive and capacitive processes. The Nyquist plot of Mn–Co LDH/rGO/$Co_2Mn_3O_8$ was recorded through EIS, as shown in Fig. 3(h). The R_{ct} value of Mn–Co LDH/rGO/$Co_2Mn_3O_8$ is 0.27 Ω, which is much lower, demonstrating fast charge-transfer kinetics and low electrolyte resistance.[60,69] The schematic of the three-electrode system utilizing Mn–Co LDH/rGO/$Co_2Mn_3O_8$ is shown in Fig. 3(i).

3.3. Mn–Co LDH/rGO/$Co_2Mn_3O_8$//AC asymmetric device fabrication

The asymmetric supercapacitor device (ASC) employing Mn–Co LDH/rGO/$Co_2Mn_3O_8$ was fabricated, as shown in Fig. 4. Fig. 4(a) shows the optimization of the potential window for the Mn–Co LDH/rGO/$Co_2Mn_3O_8$-based ASC. The CV for the ASC device was performed at different scan rates ranging from 10 to 100 mV s^{-1} in the potential range of 0 to 1.5 V. The CV shows a pseudo-rectangular shape with spikes at the borders of the potential window.

This behaviour might be attributed to the presence of rGO in Mn–Co LDH/rGO/$Co_2Mn_3O_8$. The charge–discharge analysis of the ASC device was conducted using GCD experiments in the voltage range of 0 to 1.5 V, as shown in Fig. 4(b). The specific capacitance decreases with increasing current density, as shown in Fig. 4(c). At higher current densities, the movement and transport of electrolyte ions within the electrode structure of Mn–Co LDH/rGO/$Co_2Mn_3O_8$ in the ASC device become restricted. As a result, the penetration of electrolyte ions is hindered due to the limited availability of active sites, leading to a decrease in specific capacitance at higher current densities. At higher current densities, incomplete ion diffusion leads to underutilization of the electrode surface area, thereby decreasing the specific capacitance.[70] The EIS of the ASC device is shown in Fig. 4(d). The small semicircle at the *x*-axis represents a low charge transfer resistance, which is due to fast charge-transfer kinetics. The Ragone plot (Fig. 4(e)) compares the performance of Mn–Co LDH/rGO/$Co_2Mn_3O_8$ with other ASCs reported in the literature. The Mn–Co LDH/rGO/$Co_2Mn_3O_8$-based ASC demonstrates a superior energy density of 32 Wh kg^{-1} at a power density of 600 W kg^{-1}, surpassing Mn–Co LDH/$MnCoS_4$,[71] NiMnCo-LDH,[72] $MnCo_2O_4$/NiCo-LDH,[73] and rGO@CuCo-LDH.[74] A comparison of the Mn–Co LDH/rGO/$Co_2Mn_3O_8$-based ASC supercapacitor with other ASC and zinc-ion supercapacitor devices reported in the literature is shown in Table 1.

3.4. Mn–Co LDH/rGO/$Co_2Mn_3O_8$//Zinc-ion supercapacitor device

The zinc-ion supercapacitor was fabricated by sandwiching a 2 M $ZnCl_2$-soaked filter paper between the zinc anode and the

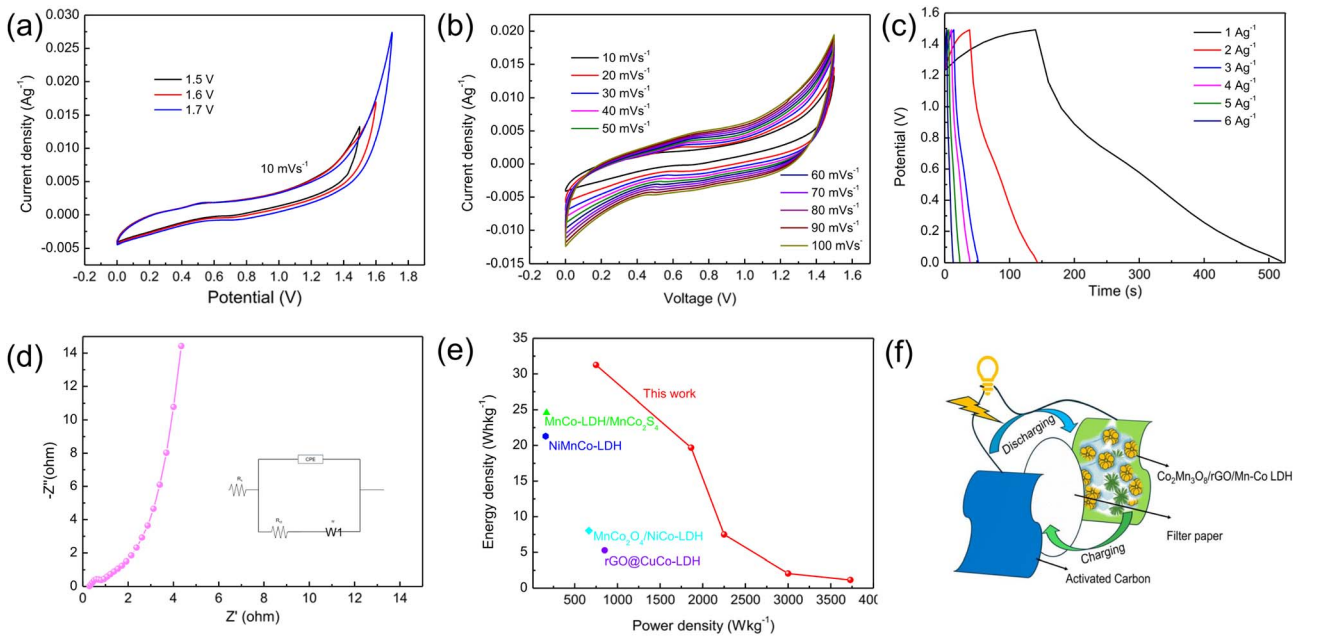

Fig. 4 ASC device testing: (a) CV curves of the ASC device at different potential windows at 10 mV s^{-1}, (b) CV curves of the ASC device at various scan rates, (c) GCD curves of the ASC device, (d) EIS spectra of the ASC device, (e) Ragone plot showing the performancecomparison of Mn–Co LDH/rGO/$Co_2Mn_3O_8$ with other supercapacitors, and (f) schematic of the ASC device.

Table 1 Comparison of the Mn–Co LDH/rGO/$Co_2Mn_3O_8$-based ASC and zinc-ion supercapcitor with other ASC and zinc-ion supercapcitor devices reported in the literature

Electrode material	Device type	Morphology	Energy density (Wh kg^{-1})	References
Mn–Co LDH/MnCoS	ASC	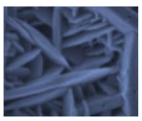	5.27	71
NiMnCo-LDH	ASC		24.6	72
$MnCo_2O_4$/NiCo-LDH	ASC	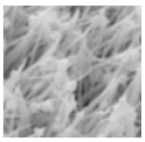	31	73
rGO@CuCo-LDH	ASC	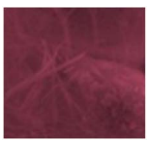	8.03	74
Mn–Co LDH/rGO/$Co_2Mn_3O_8$	ASC	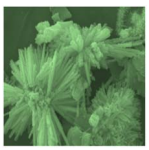	32	This study
POP-TAPP-NCTA	Zinc-ion supercapacitor	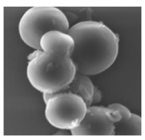	48	80
N-Ov-NCO@CC	Zinc-ion supercapacitor	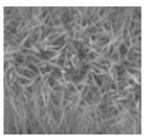	50.3	81
$H_2O/Ni^+/V_2O_5$	Zinc-ion supercapacitor	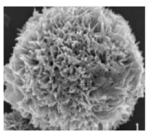	27.2	83
Mn–Co LDH/rGO/$Co_2Mn_3O_8$	This study		100	This study

as-fabricated Mn–Co LDH/rGO/$Co_2Mn_3O_8$ cathode. The effective area of both the zinc anode and the Mn–Co LDH/rGO/$Co_2Mn_3O_8$ cathode is 1 × 1 cm^2. However, to prevent short-circuiting of the electrodes, the 2 M $ZnCl_2$-soaked filter paper was cut into 2 × 1 cm^2. Fig. 5(a) shows the CV of the as-fabricated zinc-ion supercapacitor. The CV was conducted in the potential window of 0–1.2 V at different scan rates from 10 to 100 mV s^{-1}, showing a quasi-pseudocapacitive shape with cathodic peaks at 0.35 V and anodic peaks at 0.85 V. These peaks result from the interaction of Mn and Co ions with Zn^{2+} ions.[75] As a result, the specific capacitance is increased compared to the ASC device counterparts. Furthermore, the CV peaks do not shift with different scan rates, which indicates fast charge-transfer kinetics and minimal polarization.[76] The Dunn's method was also used to analyze the CV curves of Mn–Co LDH/rGO/$Co_2Mn_3O_8$:[77]

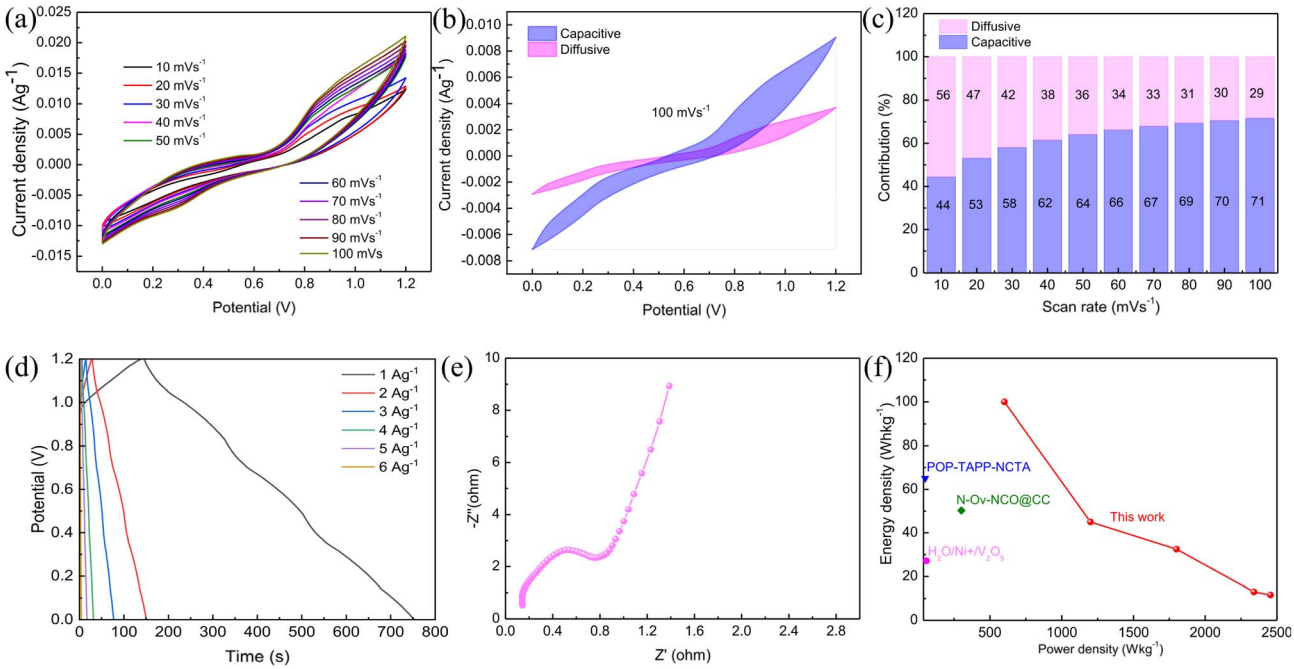

Fig. 5 Zinc-ion supercapacitor device testing based on Mn–Co LDH/rGO/$Co_2Mn_3O_8$: (a) CV curves of the zinc-ion supercapacitor device at different scan rates, (b) capacitive *vs.* diffusive contributions of zinc-ion supercapcitor device at 100 mV s^{-1}, (c) the Dunn's method analysis of the zinc-ion supercapacitor, (d) GCD curves of the zinc-ion supercapacitor, (e) EIS spectra of the zinc-ion supercapacitor and (f) the Ragone plot of zinc-ion supercapacitor showing the comparison with other zinc-ion supercapacitors.

$$I(V) = k_1 v + k_2 v^{\left(\frac{1}{2}\right)}$$

The $k_1 v$ term represents the capacitive contribution, while $k_2 v^{\frac{1}{2}}$ term represents the diffusive contribution. The capacitive contributions were 44%, 53%, 58%, 62%, 64%, 66%, 67%, 69%, 70%, and 71% at scan rates of 10, 20, 30, 40, 50, 60, 70, 80, 90, and 100 mV s^{-1}, respectively. Correspondingly, the diffusive contributions were 56%, 47%, 42%, 38%, 36%, 34%, 33%, 31%, 30%, and 29% at the same scan rates, as shown in Fig. 5(b). Furthermore, the diffusive and capacitive contributions at a scan rate of 100 mV s^{-1} show that the capacitive contribution (71%) dominates the diffusive contribution (29%), reflecting that charge transfer is governed by a surface-controlled mechanism and is highly reversible, as shown in Fig. 5(c).[65] The GCD was performed for the zinc-ion supercapacitor in the potential window of 0 to 1.2 V, as shown in Fig. 5(d). The humps in the GCD further confirm the redox reactions associated with the intercalation and deintercalation of zinc ions in Mn–Co LDH/rGO/$Co_2Mn_3O_8$. The Nyquist plot of the zinc-ion supercapacitor device is shown in Fig. 5(e).

The semicircle in the high-frequency region represents charge transfer resistance.[78] The lower R_{ct} value of 0.6 Ω reflects the fast charge transfer kinetics of Zn^{2+} ion intercalation and deintercalation due to the rosette-like and nanoflower-like morphologies present in Mn–Co LDH/rGO/$Co_2Mn_3O_8$. The straight line in the lower-frequency region represents the Warburg impedance.[79] Furthermore, the Ragone plot shows a comparison of the energy density and power density performance with the reported literature, as shown in Fig. 5(f). The Mn–Co LDH/rGO/$Co_2Mn_3O_8$ electrode successfully achieved an energy density of 100 Wh kg^{-1} at a power density of 780 W kg^{-1}. This represents a significant increase in energy density compared to traditional asymmetric supercapacitors (ASCs). Furthermore, the Mn–Co LDH/rGO/$Co_2Mn_3O_8$ electrode for zinc-ion supercapacitors demonstrates significantly superior performance in both energy density and power density when compared to other electrode materials, such as POP-TAPP-NCTA,[80] N-Ov-NCO@CC,[81] and $H_2O/Ni^+/V_2O_5$,[82] which have also been used as cathodes in zinc-ion supercapacitors. A comparison of the Mn–Co LDH/rGO/$Co_2Mn_3O_8$-based zinc-ion supercapacitor with other ASC and zinc-ion supercapacitor devices reported in the literature is shown in Table 1.

3.5. OER

The Mn–Co LDH/rGO/$Co_2Mn_3O_8$ was also explored for OER activity due to its hierarchical morphology. The OER electrochemical characterization was performed in 0.1 M KOH using a three-electrode system employing Mn–Co LDH/rGO/$Co_2Mn_3O_8$. The platinum foil and Ag/AgCl served as the counter electrode and reference electrode, respectively. All potentials recorded on Ag/AgCl were converted to the reversible hydrogen electrode (RHE) scale using the Nernst equation:[84]

$$E = E_{Ag/AgCl} + 0.197 + 0.059 \times pH$$

Furthermore, the Tafel slope was calculated using the following equation:[85]

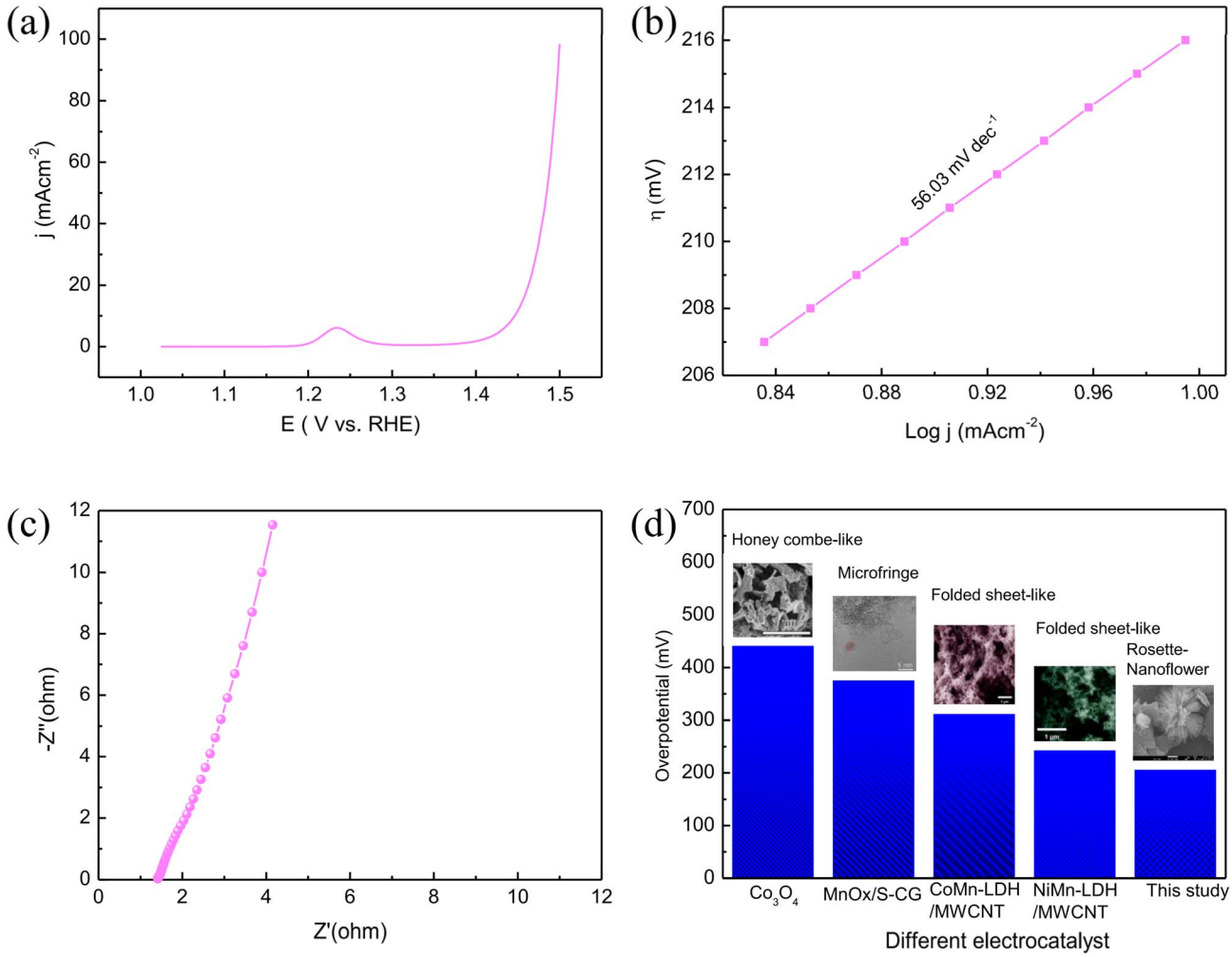

Fig. 6 OER evaluation of Mn–Co LDH/rGO/$Co_2Mn_3O_8$: (a) LSV curve of Mn–Co LDH/rGO/$Co_2Mn_3O_8$ at 10 mV s^{-1}, (b) Tafel slope of Mn–Co LDH/rGO/$Co_2Mn_3O_8$, (c) EIS spectra of Mn–Co LDH/rGO/$Co_2Mn_3O_8$, and (d) comparison of the overpotential of Mn–Co LDH/rGO/$Co_2Mn_3O_8$ with that of the other electrocatalysts reported in the literature.

$$\eta = a + b\log(j)$$

η represents the overpotential in mV j represents the current density in $mAcm^{-2}$. a is a constant. b represents the Tafel slope in mV dec^{-1}.

The LSV was performed in the potential window of 0 to 1.5 V *vs.* RHE at a scan rate of 10 mV s^{-1}, as shown in Fig. 6(a). The LSV curve begins to rise at 1.3 V *vs.* RHE, which corresponds to the onset potential. This indicates the electrocatalytic activity of Mn–Co LDH/rGO/$Co_2Mn_3O_8$. The overpotential calculated at 10 mA cm^{-2} was found to be 218 mV. The Tafel slope was calculated using the Nernst equation. The Mn–Co LDH/rGO/$Co_2Mn_3O_8$ shows a low Tafel slope of 56.03 mV dec^{-1}, as shown in Fig. 6(b). The low overpotential and Tafel slope of Mn–Co LDH/rGO/$Co_2Mn_3O_8$ indicate that the hierarchical morphology, resulting from the nanoflowers of Mn–Co LDH integrated with the rosette-like $Co_2Mn_3O_8$, provides abundant active sites. This enhances the electrocatalytic activity and kinetics of Mn–Co LDH/rGO/$Co_2Mn_3O_8$ for the OER. Mn–Co LDH/rGO/$Co_2Mn_3O_8$ outperforms the other electrocatalysts reported in the literature.

The EIS was also performed for Mn–Co LDH/rGO/$Co_2Mn_3O_8$, as shown in Fig. 6(c).[86] The semicircle in the higher frequency region represents R_{ct}. The low charge-transfer resistance reflects the increased electrocatalytic activity of Mn–Co LDH/rGO/$Co_2Mn_3O_8$ for the OER.

Fig. 6(d) shows the comparison of the overpotential of Mn–Co LDH/rGO/$Co_2Mn_3O_8$ with various electrocatalysts reported in the literature. Mn–Co LDH/rGO/Co_2Mn_3O with an overpotential of 218 mV outperforms the $Co_3O_{4-\delta}$ quantum dots,[87] MnO_x/S-GC, Co_5Mn-LDH/MWCNT,[88] and Ni_5Mn-LDH/MWCNT.[88]

4. Conclusion

In conclusion, a unique rosette-like $Co_2Mn_3O_8$ was synthesized and integrated with nanoflower-like Mn–Co LDH through rGO. Mn–Co LDH/rGO/$Co_2Mn_3O_8$ was prepared *via* hydrothermal synthesis, followed by calcination, exhibiting a high specific capacitance of 2500 F g^{-1} at 1 A g^{-1}. Additionally, an asymmetric supercapacitor (ASC) employing Mn–Co LDH/rGO/

$Co_2Mn_3O_8$ demonstrated superior performance with an energy density of 32 Wh kg^{-1} at a power density of 600 W kg^{-1}. The zinc-ion supercapacitor based on Mn–Co LDH/rGO/$Co_2Mn_3O_8$ showed even better electrochemical performance. The energy and power density of the zinc-ion supercapacitor employing Mn–Co LDH/rGO/$Co_2Mn_3O_8$ were significantly improved with an energy density of 100 Wh kg^{-1} at a power density of 780 W kg^{-1}. Furthermore, the OER activity of Mn–Co LDH/rGO/$Co_2Mn_3O_8$ was evaluated in 0.1 M KOH, showing a low overpotential of 218 mV and a Tafel slope of 56.03 mV dec^{-1}. The bifunctional capability of Mn–Co LDH/rGO/$Co_2Mn_3O_8$ for both supercapacitors and OER arises from its unique rosette-like and nanoflower morphology, which enhances charge transport and reduces electrolyte resistance. This study provides a comprehensive strategy for addressing energy storage and conversion using bifunctional materials.

Conflicts of interest

The authors declare no competing interests.

Data availability

All data supporting the findings of this study are included in the manuscript.

Acknowledgements

The authors acknowledge the support provided by United Arab Emirates University (UAEU) funding No. 12N141.

References

1 S. S. A. Shah, *et al.*, Recent advances on oxygen reduction electrocatalysis: Correlating the characteristic properties of metal organic frameworks and the derived nanomaterials, *Appl. Catal., B*, 2020, **268**, 118570, DOI: 10.1016/J.APCATB.2019.118570.

2 M. Waseem, M. Al-Marzouqi and N. Ghasem, Enhancing regeneration energy efficiency of CO2-rich amine solution with a novel tri-composite catalyst, *J. CO_2 Util.*, 2024, **82**, 102764, DOI: 10.1016/J.JCOU.2024.102764.

3 S. M. Allah, M. K. Aslam, I. Hussain, F. M. Hassan, A. Al-Marzouqi and M. Xu, Ultra-high-performance zinc-ion supercapacitor based on single-copper molybdate urchins, *J. Energy Storage*, 2025, **131**, 117610, DOI: 10.1016/J.EST.2025.117610.

4 M. Waseem, N. Ghasem and M. Al-Marzouqi, Advances in hollow fiber membrane contactors for CO2 stripping, *Mater. Today Sustain.*, 2025, **29**, 101056, DOI: 10.1016/j.mtsust.2024.101056.

5 M. Waseem, M. S. Shah, N. Ghasem and M. Al-Marzouqi, CO_2 stripping from amine solutions using PES hollow fiber membrane contactors, *J. Environ. Chem. Eng.*, 2026, **14**(1), 121101, DOI: 10.1016/J.JECE.2026.121101.

6 S. Mehmood, *et al.*, Semiconducting metal oxides-based electrodes as the photoanodes of dye-sensitized solar cells (DSSCs), *Dye-Sensitized Sol. Cells*, 2022, 103–136, DOI: 10.1016/B978-0-12-818206-2.00004-9.

7 M. Waseem, N. Ghasem and M. Al-Marzouqi, Experimental and simulation study of a catalytic-membrane integrated system for efficient CO2 stripping, *Chem. Eng. Process. Process Intensif.*, 2025, **211**, 110216, DOI: 10.1016/j.cep.2025.110216.

8 R. K. Raji, T. Ramachandran, J. S. Punitha, U. Ahmed and F. Hamed, Structural and functional analysis of Eu3+-doped Sr2FeTiO6 perovskites: insights into electrical and magnetic characteristics, *J. Mater. Sci.: Mater. Electron.*, 2025, **36**(2), 1–18, DOI: 10.1007/S10854-024-14173-0/FIGURES/4.

9 S. Min Allah, A. H. Al-Marzouqi and F. M. Hassan, Advancements in electrocatalyst for electrocatalytic conversion of carbon dioxide to methane, *Mater. Today Sustain.*, 2024, **27**, 100817, DOI: 10.1016/J.MTSUST.2024.100817.

10 M. F. Siddique, F. K. Omar, M. Waseem and A. H. Al-Marzouqi, Self-Cleaning Alginate–PVA Hydrogel Evaporator with Enhanced Solar Desalination Efficiency and Long-Term Salt Resistance, *ACS Omega*, 2025, **10**(44), 52459–52472, DOI: 10.1021/ACSOMEGA.5C05414/SUPPL_FILE/AO5C05414_SI_002.MP4.

11 W. Dong, *et al.*, Deep insight into the differences in alkali stability and electrochemical performance of NiCo sulfides, *Electrochim. Acta*, 2025, **543**, 147619, DOI: 10.1016/J.ELECTACTA.2025.147619.

12 M. K. Aslam, *et al.*, Sulfur encapsulation into yolk-shell Fe2N@nitrogen doped carbon for ambient-temperature sodium-sulfur battery cathode, *Chem. Eng. J.*, 2022, **429**, 132389, DOI: 10.1016/J.CEJ.2021.132389.

13 N. Saberi, M. A. Vaziri Rad, K. Zamanpour and A. Kasaeian, Comparative techno-economic analysis of battery bank and integrated flywheel and generator in a hybrid renewable system under tropical climate, *J. Energy Storage*, 2024, **103**, 114145, DOI: 10.1016/J.EST.2024.114145.

14 S. Li, *et al.*, Propelling polysulfide conversion for high-loading lithium–sulfur batteries through highly sulfiphilic NiCo2S4 nanotubes, *Energy Storage Mater.*, 2020, **27**, 51–60, DOI: 10.1016/J.ENSM.2020.01.017.

15 S. M. Allah, A. H. Al-Marzouqi, F. M. Hassan, M. K. Aslam, A. Riaz and I. Hussain, Controlled morphological synthesis of carbon nanotube-enhanced bismuth metal-organic frameworks: A promising electrode material for supercapacitors, *Electrochim. Acta*, 2025, **531**, 146454, DOI: 10.1016/J.ELECTACTA.2025.146454.

16 S. Mehmood, *et al.*, Sonochemically synthesized structures of manganese oxide (MO): A cathode material for oxygen reduction reaction in fuel cell applications, *Int. J. Hydrogen Energy*, 2024, **52**, 1254–1263, DOI: 10.1016/J.IJHYDENE.2023.11.166.

17 H. H. Shanaah, *et al.*, Cobalt-doped graphitic carbon nitride: A multifunctional material for humidity sensing, electrochemical water splitting and environmental remediation applications, *J. Alloys Compd.*, 2024, **1008**, 176498, DOI: 10.1016/J.JALLCOM.2024.176498.

18 L. Li, *et al.*, NiFe-LDH modified cobalt boride for enhanced OER catalytic performance, *Electrochim. Acta*, 2025, **539**, 147094, DOI: 10.1016/J.ELECTACTA.2025.147094.
19 C. Jing, *et al.*, Curvature-dominated microenvironment modulation enables efficient electrocatalytic oxygen reduction, *Nano Res.*, 2026, **19**(1), 94908197, DOI: 10.26599/NR.2025.94908197.
20 S. Li, *et al.*, Vanadium dioxide–reduced graphene oxide binary host as an efficient polysulfide plague for high-performance lithium–sulfur batteries, *J. Mater. Chem. A*, 2019, **7**(4), 1658–1668, DOI: 10.1039/C8TA10422K.
21 N. Sonadia, Z. Iqbal, W. Miran, A. Ul-Hamid, K. S. Ayub and F. Azad, Enhanced Electrocatalytic Performance of Erbium-Incorporated Nickel-Based Metal-Organic Frameworks for Water Splitting, *Energy Fuels*, 2024, **38**(6), 5397–5406, DOI: 10.1021/ACS.ENERGYFUELS.3C04609/SUPPL_FILE/EF3C04609_SI_001.PDF.
22 M. S. Javed, *et al.*, High-performance flexible hybrid-supercapacitor enabled by pairing binder-free ultrathin Ni–Co–O nanosheets and metal-organic framework derived N-doped carbon nanosheets, *Electrochim. Acta*, 2020, **349**, 136384, DOI: 10.1016/J.ELECTACTA.2020.136384.
23 C. Jing, *et al.*, Layered double hydroxide-based nanomaterials for supercapacitors and batteries: Strategies and mechanisms, *Prog. Mater. Sci.*, 2025, **150**, 101410, DOI: 10.1016/J.PMATSCI.2024.101410.
24 Y. Zhang, *et al.*, Trimetallic layered double hydroxides with a hierarchical heterostructure for high-performance supercapcitors, *J. Energy Storage*, 2023, **61**, 106700, DOI: 10.1016/J.EST.2023.106700.
25 M. Aman, *et al.*, Layered double hydroxide based composites for energy storage applications: Insights into supercapacitors and batteries, *J. Energy Storage*, 2025, **116**, 116093, DOI: 10.1016/J.EST.2025.116093.
26 P. S. Dighe, R. S. Redekar, N. L. Tarwal and P. B. Sarawade, Design and development of the high-performance aqueous asymmetric supercapacitor based on the hydrothermally grown binder-less Ni-Co LDH nanosheets, *J. Energy Storage*, 2024, **88**, 111467, DOI: 10.1016/J.EST.2024.111467.
27 C. Jing, *et al.*, Construction of MoB@LDH heterojunction and its derivates through phase and interface engineering for advanced supercapacitor applications, *J. Colloid Interface Sci.*, 2024, **660**, 10–20, DOI: 10.1016/J.JCIS.2023.12.184.
28 Q. Lv, *et al.*, Iron (III)-Facilitated reconstruction in NiMn layered double hydroxides for initiating rapid oxygen evolution reaction, *Int. J. Hydrogen Energy*, 2024, **92**, 1266–1275, DOI: 10.1016/J.IJHYDENE.2024.09.257.
29 M. Moradi, A. Afkhami, T. Madrakian and H. R. Moazami, Electrosynthesis of CoMn layered-double-hydroxide as a precursor for Co-Mn-MOFs and subsequent electrochemical sulfurization for supercapacitor application, *J. Energy Storage*, 2023, **71**, 108177, DOI: 10.1016/J.EST.2023.108177.
30 Z. Xu, *et al.*, Mn-doped NiCo LDH nanosheets with rich oxygen vacancies for high-performance supercapacitors and efficient oxygen evolution, *J. Energy Storage*, 2025, **106**, 114848, DOI: 10.1016/J.EST.2024.114848.
31 U. Draz, M. Waseem and T. Iqbal, Characterization and corrosion analysis of zinc coating by electrodeposition using acid chloride electrolyte solution, *Results Surf. Interfaces*, 2025, **20**, 100588, DOI: 10.1016/J.RSURFI.2025.100588.
32 D. Su, *et al.*, Co, Mn-LDH nanoneedle arrays grown on Ni foam for high performance supercapacitors, *Appl. Surf. Sci.*, 2019, **469**, 487–494, DOI: 10.1016/J.APSUSC.2018.10.276.
33 H. Xuan, *et al.*, Hierarchical MnCo-LDH/rGO@NiCo2S4 heterostructures on Ni foam with enhanced electrochemical properties for battery-supercapacitors, *Electrochim. Acta*, 2020, **335**, 135691, DOI: 10.1016/J.ELECTACTA.2020.135691.
34 S. Liu, *et al.*, Hierarchical MnCo-layered double hydroxides@Ni(OH)2 core–shell heterostructures as advanced electrodes for supercapacitors, *J. Mater. Chem. A*, 2017, **5**(3), 1043–1049, DOI: 10.1039/C6TA07842G.
35 R. Zainul, *et al.*, Advanced OER catalysts: MnCo-LDH integrated with NiP2 and Ni5P4 metal phosphides for superior water splitting performance, *Appl. Clay Sci.*, 2025, **275**, 107868, DOI: 10.1016/J.CLAY.2025.107868.
36 G. Ma, M. Qin, W. Tan, Z. Fan and X. Xin, Optimizing OER performance with CoFe-LDH@MnCo–CH nanoneedle arrays: Leveraging p–n junctions in electrocatalysis, *Int. J. Hydrogen Energy*, 2024, **60**, 902–908, DOI: 10.1016/J.IJHYDENE.2024.01.363.
37 Z. Li, K. Xiao, C. Yu, H. Wang and Q. Li, Three-dimensional graphene-like carbon nanosheets coupled with MnCo-layered double hydroxides nanoflowers as efficient bifunctional oxygen electrocatalyst, *Int. J. Hydrogen Energy*, 2021, **46**(69), 34239–34251, DOI: 10.1016/J.IJHYDENE.2021.07.221.
38 H. Wu, X. Xie, Z. Sun and P. Du, Synergistic Effect in NiCoP@NiCoMn-LDH Core–Shell Heterostructures for High-Performance Supercapacitor, *Electrochim. Acta*, 2025, 147268, DOI: 10.1016/J.ELECTACTA.2025.147268.
39 T. Shaikh, S. Pise, O. Kulkarni, R. Sankannavar, C. Jambhale and S. Kolekar, Designing of bimetallic rGO@Co/Mn MOF and bioderived carbon as efficient electrodes for high-performance asymmetric supercapacitor, *J. Energy Storage*, 2025, **112**, 115545, DOI: 10.1016/J.EST.2025.115545.
40 Y. Sang, Z. Guo, G. Li, Y. Xue and J. Xue, Enhanced water electrolysis activity by CoNi-LDH/Co -nitrogen-doped carbon heterostructure with dual catalytic active sites, *Electrochim. Acta*, 2023, **444**, 141956, DOI: 10.1016/J.ELECTACTA.2023.141956.
41 S. Tian, Y. Wang, W. Gao, J. Sun, J. Zhang and X. Zhang, One-step electrodeposition of CoMn-LDH with core-shell configuration for enhancing charge storage capabilities of on-chip microsupercapacitor, *Electrochim. Acta*, 2025, **539**, 146660, DOI: 10.1016/J.ELECTACTA.2025.146660.
42 F. Yan, *et al.*, Fast fabrication of ultrathin CoMn LDH nanoarray as flexible electrode for water oxidation,

Electrochim. Acta, 2018, **283**, 755–763, DOI: 10.1016/J.ELECTACTA.2018.06.202.

43 C. Zhang, *et al.*, Introduction of bimetallic oxide-modified carbon nanotubes for boosting the energy storage performance of NiCo-LDH based in-plane micro-supercapacitors on paper, *Chem. Eng. J.*, 2024, **494**, 153242, DOI: 10.1016/J.CEJ.2024.153242.

44 J. L. Patil, *et al.*, Fabrication of chrysanthemum-flower-like $CuMoO_4$ electrodes for high performance supercapacitor applications, *Inorg. Chem. Commun.*, 2025, **182**, 115319, DOI: 10.1016/J.INOCHE.2025.115319.

45 S. M. Allah, M. K. Aslam, I. Hussain, F. M. Hassan, A. Al-Marzouqi and M. Xu, Ultra-high-performance zinc-ion supercapacitor based on single-copper molybdate urchins, *J. Energy Storage*, 2025, **131**, 117610, DOI: 10.1016/J.EST.2025.117610.

46 P. B. Perroni, T. V. B. Ferraz, J. Rousseau, C. Canaff, H. Varela and T. W. Napporn, Stainless steel supported NiCo2O4 active layer for oxygen evolution reaction, *Electrochim. Acta*, 2023, **453**, 142295, DOI: 10.1016/J.ELECTACTA.2023.142295.

47 J. Jiang, X. L. Zhou, H. G. Lv, H. Q. Yu and Y. Yu, Bimetallic-Based Electrocatalysts for Oxygen Evolution Reaction, *Adv. Funct. Mater.*, 2023, **33**(10), 2212160, DOI: 10.1002/ADFM.202212160.

48 A. Ramadan, *et al.*, Fabrication of Co2Mn3O8@NiMnLDH nanocomposite array on nickel foam for oxygen evaluation reaction, *Inorg. Chem. Commun.*, 2023, **152**, 110670, DOI: 10.1016/J.INOCHE.2023.110670.

49 C. Ye, P. Fan, D. Wei, J. Wang and L. Xu, Nitrogen-doped carbon fibers loaded with Co/Co2Mn3O8 alloy nanoparticles as bifunctional oxygen electrocatalysts for rechargeable zinc-air batteries, *J. Alloys Compd.*, 2023, **936**, 168210, DOI: 10.1016/J.JALLCOM.2022.168210.

50 Y. Lei, Q. Wang, S. Peng, S. Ramakrishna, D. Zhang and K. Zhou, Electrospun Inorganic Nanofibers for Oxygen Electrocatalysis: Design, Fabrication, and Progress, *Adv. Energy Mater.*, 2020, **10**(45), 1902115, DOI: 10.1002/AENM.201902115.

51 N. M. S. Hidayah, *et al.*, Comparison on graphite, graphene oxide and reduced graphene oxide: Synthesis and characterization, *AIP Conf. Proc.*, 2017, **1892**(1), DOI: 10.1063/1.5005764/965987.

52 K. Sarmah, J. Pal, T. K. Maji and S. Pratihar, Magnetically Recoverable Heterobimetallic Co2Mn3O8: Selective and Sustainable Oxidation and Reduction Reactions, *ACS Sustain. Chem. Eng.*, 2017, **5**(12), 11504–11515, DOI: 10.1021/ACSSUSCHEMENG.7B02739/ASSET/IMAGES/MEDIUM/SC-2017-02739Q_0016.GIF.

53 B. Li, L. Dai, G. L. Su, Z. Xia, Y. Ye and Z. Li, Construction of defective MnCo-LDH nanoflowers with high activity for overall water splitting, *Fuel*, 2024, **364**, 130961, DOI: 10.1016/J.FUEL.2024.130961.

54 Y. Guo, S. Zhang, J. Wang, Z. Liu and Y. Liu, Facile preparation of high-performance cobalt–manganese layered double hydroxide/polypyrrole composite for battery-type asymmetric supercapacitors, *J. Alloys Compd.*, 2020, **832**, 154899, DOI: 10.1016/J.JALLCOM.2020.154899.

55 N. Bayat, I. M. Szilágyi, J. Madarász, B. L. Károly and A. Farkas, Thermal decomposition of hexaamminecobalt (III) dibromide permanganate: Formation of cobalt-manganese oxide spinel and catalytically active intermediates, *Inorg. Chem. Commun.*, 2025, **179**, 114852, DOI: 10.1016/J.INOCHE.2025.114852.

56 A. Y. Lee, *et al.*, Raman study of D* band in graphene oxide and its correlation with reduction, *Appl. Surf. Sci.*, 2021, **536**, 147990, DOI: 10.1016/J.APSUSC.2020.147990.

57 B. Li, L. Dai, G. L. Su, Z. Xia, Y. Ye and Z. Li, Construction of defective MnCo-LDH nanoflowers with high activity for overall water splitting, *Fuel*, 2024, **364**, 130961, DOI: 10.1016/J.FUEL.2024.130961.

58 H. A. Hamouda, *et al.*, High-performance asymmetric supercapacitor based on urchin-like cobalt manganese oxide nanoneedles and biomass-derived carbon nanosheet electrode materials, *J. Energy Storage*, 2022, **47**, 103616, DOI: 10.1016/J.EST.2021.103616.

59 F. T. Johra and W. G. Jung, Hydrothermally reduced graphene oxide as a supercapacitor, *Appl. Surf. Sci.*, 2015, **357**, 1911–1914, DOI: 10.1016/J.APSUSC.2015.09.128.

60 M. Li, J. P. Cheng, J. Wang, F. Liu and X. B. Zhang, The growth of nickel-manganese and cobalt-manganese layered double hydroxides on reduced graphene oxide for supercapacitor, *Electrochim. Acta*, 2016, **206**, 108–115, DOI: 10.1016/J.ELECTACTA.2016.04.084.

61 X. Gao, *et al.*, Significant Role of Al in Ternary Layered Double Hydroxides for Enhancing Electrochemical Performance of Flexible Asymmetric Supercapacitor, *Adv. Funct. Mater.*, 2019, **29**(36), 1903879, DOI: 10.1002/ADFM.201903879.

62 M. Ramadan, A. M. Abdellah, S. G. Mohamed and N. K. Allam, 3D Interconnected Binder-Free Electrospun MnO@C Nanofibers for Supercapacitor Devices, *Sci. Rep.*, 2018, **8**(1), 1–8, DOI: 10.1038/S41598-018-26370-Z.

63 J. Yu, *et al.*, High Specific Capacitance Electrode Material for Supercapacitors Based on Resin-Derived Nitrogen-Doped Porous Carbons, *ACS Omega*, 2019, **4**(14), 15904–15911, DOI: 10.1021/ACSOMEGA.9B01916/ASSET/IMAGES/MEDIUM/AO9B01916_M004.GIF.

64 K. Kannadasan, V. Sankar Devi, S. Archana, P. Thomas and P. Elumalai, Deconvolution of capacitive and diffusive charge/lithium storage in lyophilized NiCo2S4–NiCo2O4 composite for supercapattery and lithium-ion battery, *New J. Chem.*, 2023, **47**(29), 13963–13978, DOI: 10.1039/D3NJ01663C.

65 L. Guan, L. Yu and G. Z. Chen, Capacitive and non-capacitive faradaic charge storage, *Electrochim. Acta*, 2016, **206**, 464–478, DOI: 10.1016/J.ELECTACTA.2016.01.213.

66 S. M. Allah, M. K. Aslam, I. Hussain, F. M. Hassan, A. Al-Marzouqi and M. Xu, Ultra-high-performance zinc-ion supercapacitor based on single-copper molybdate urchins, *J. Energy Storage*, 2025, **131**, 117610, DOI: 10.1016/J.EST.2025.117610.

67 Y. Wu, Y. Deng, K. Zhang, J. Qiu, J. Wu and L. Yan, Ultrahigh Conductive and Stretchable Eutectogel Electrolyte for High-Voltage Flexible Antifreeze Quasi-solid-state Zinc-Ion

Hybrid Supercapacitor, *ACS Appl. Energy Mater.*, 2022, **5**(3), 3013–3021, DOI: 10.1021/ACSAEM.1C03654/ASSET/IMAGES/MEDIUM/AE1C03654_M005.GIF.

68 C. Xu, *et al.*, Large-area high-quality 2D ultrathin Mo2C superconducting crystals, *Nat. Mater.*, 2015, **14**(11), 1135–1141, DOI: 10.1038/NMAT4374.

69 A. Ramadan, *et al.*, Fabrication of Co2Mn3O8@NiMnLDH nanocomposite array on nickel foam for oxygen evaluation reaction, *Inorg. Chem. Commun.*, 2023, **152**, 110670, DOI: 10.1016/J.INOCHE.2023.110670.

70 P. S. Kumar, J. Bae, J. W. Roh, Y. Min and S. Lee, Enhanced voltage and capacitance in flexible supercapacitors using electrospun nanofiber electrolytes and CuNi2O3@N-Doped omnichannel carbon electrodes, *Nano Convergence*, 2025, **12**(1), 21, DOI: 10.1186/S40580-025-00485-2.

71 A. S. Raja, R. Sasikumar, S. M. Chen and B. Kim, Unveiling the Synergistic Effect of MnCo LDH Adorned MnCo2S4 Nanocomposite as Efficient Bifunctional Electrode for Asymmetric Supercapacitor and Overall Water Splitting, *Small*, 2025, **21**(29), e2411728, DOI: 10.1002/SMLL.202411728.

72 A. Zhang, Q. Zhang, J. Huang, H. Fu, H. Zong and H. Guo, NiMnCo-LDH in-situ derived from ZIF-67@ZnO as self-supporting electrode for asymmetric supercapacitor device, *Chem. Eng. J.*, 2024, **487**, 150587, DOI: 10.1016/J.CEJ.2024.150587.

73 J. J. Zhou, *et al.*, Shish-kebab type MnCo2O4@Co3O4 nanoneedle arrays derived from MnCo-LDH@ZIF-67 for high-performance supercapacitors and efficient oxygen evolution reaction, *Chem. Eng. J.*, 2018, **354**, 875–884, DOI: 10.1016/J.CEJ.2018.08.102.

74 R. Sankannavar, R. Bhosale, R. Kangutkar, S. Kolekar and J. Manjanna, Facile synthesis of a rGO@CuCo-layered double hydroxide electrode for a high-performance solid-state symmetric supercapacitor, *J. Energy Storage*, 2024, **94**, 112455, DOI: 10.1016/J.EST.2024.112455.

75 X. Zhou, W. Yang, C. Wu, S. Li and L. Li, Zinc-Ion Hybrid Supercapacitors: A Review on Electrode Materials, Electrolytes, and Diaphragms to Inhibit Zinc Dendrite Growth, *Energy Fuels*, 2025, **39**(21), 9641–9667, DOI: 10.1021/ACS.ENERGYFUELS.4C05246/ASSET/IMAGES/LARGE/EF4C05246_0026.JPEG.

76 S. K. Meher and G. R. Rao, Ultralayered Co3O4 for high-performance supercapacitor applications, *J. Phys. Chem. C*, 2011, **115**(31), 15646–15654, DOI: 10.1021/JP201200E/SUPPL_FILE/JP201200E_SI_001.

77 M. Barazandeh and S. H. Kazemi, High-performance freestanding supercapacitor electrode based on polypyrrole coated nickel cobalt sulfide nanostructures, *Sci. Rep.*, 2022, **12**(1), 1–13, DOI: 10.1038/s41598-022-08691-2.

78 R. Weber, A. J. Louli, K. P. Plucknett and J. R. Dahn, Resistance Growth in Lithium-Ion Pouch Cells with LiNi 0.80 Co 0.15 Al 0.05 O 2 Positive Electrodes and Proposed Mechanism for Voltage Dependent Charge-Transfer Resistance, *J. Electrochem. Soc.*, 2019, **166**(10), A1779–A1784, DOI: 10.1149/2.0361910JES/DATA.

79 A. A. Moya, Low-frequency approximations to the finite-length Warburg diffusion impedance: The reflexive case, *J. Energy Storage*, 2024, **97**, 112911, DOI: 10.1016/J.EST.2024.112911.

80 F. Z. Cui, *et al.*, Polyarylimide and porphyrin based polymer microspheres for zinc ion hybrid capacitors, *Chem. Eng. J.*, 2021, **405**, 127038, DOI: 10.1016/J.CEJ.2020.127038.

81 X. Zhang, *et al.*, Synergistic effects of defects and surface engineering in Ni-Co metal oxides to improve the high performance of Zn-ion hybrid supercapacitors, *J. Energy Storage*, 2024, **86**, 111208, DOI: 10.1016/J.EST.2024.111208.

82 X. Liang, J. Li, X. Yang, L. Wang, X. Li and W. Lü, H2O/Ni2+ intercalated lamellar vanadium oxide as cathode materials for aqueous zn-ion hybrid supercapacitors, *J. Energy Storage*, 2022, **56**, 105947, DOI: 10.1016/J.EST.2022.105947.

83 X. Liang, J. Li, X. Yang, L. Wang, X. Li and W. Lü, H2O/Ni2+ intercalated lamellar vanadium oxide as cathode materials for aqueous zn-ion hybrid supercapacitors, *J. Energy Storage*, 2022, **56**, 105947, DOI: 10.1016/J.EST.2022.105947.

84 L. Wang, C. Y. Lee and P. Schmuki, Solar water splitting: preserving the beneficial small feature size in porous α-Fe2O3 photoelectrodes during annealing, *J. Mater. Chem. A*, 2012, **1**(2), 212–215, DOI: 10.1039/C2TA00431C.

85 O. van der Heijden, S. Park, R. E. Vos, J. J. J. Eggebeen and M. T. M. Koper, Tafel Slope Plot as a Tool to Analyze Electrocatalytic Reactions, *ACS Energy Lett.*, 2024, **9**(4), 1871–1879, DOI: 10.1021/ACSENERGYLETT.4C00266/ASSET/IMAGES/LARGE/NZ4C00266_0004.JPEG.

86 D. Su, *et al.*, Co, Mn-LDH nanoneedle arrays grown on Ni foam for high performance supercapacitors, *Appl. Surf. Sci.*, 2019, **469**, 487–494, DOI: 10.1016/J.APSUSC.2018.10.276.

87 G. Zhang, J. Yang, H. Wang, H. Chen, J. Yang and F. Pan, Co3O4-δ Quantum Dots As a Highly Efficient Oxygen Evolution Reaction Catalyst for Water Splitting, *ACS Appl. Mater. Interfaces*, 2017, **9**(19), 16159–16167, DOI: 10.1021/ACSAMI.7B01591/ASSET/IMAGES/LARGE/AM-2017-01591H_0007.

88 G. Jia, *et al.*, Formation of Hierarchical Structure Composed of (Co/Ni)Mn-LDH Nanosheets on MWCNT Backbones for Efficient Electrocatalytic Water Oxidation, *ACS Appl. Mater. Interfaces*, 2016, **8**(23), 14527–14534, DOI: 10.1021/ACSAMI.6B02733/ASSET/IMAGES/LARGE/AM-2016-02733H_0007.JPEG.